Journal of Applied Fluid Mechanics, Vol. 17, No. 9, pp. 1860-1873, 2024.
Available online at www.jafmonline.net, ISSN 1735-3572, EISSN 1735-3645.
https://doi.org/10.47176/jafm.17.9.2564

Numerical Study on the Hydrodynamic Coefficients and Flow Field Characteristics of Underwater Manipulator

S. Dai[1], S. Ren[2], X. Liu[3], D. Duan[1†], H. Jin[1] and H. Zhang[1]

[1] *School of Mechanical Engineering, University of Jinan, Jinan, 250022, China*
[2]*Bei qi Foton Motor Co., Ltd., Weifang, 262200, China*
[3]*Zibo Non-public Sector Development Center, Zibo, 255000, China*

†*Corresponding Author Email: me_duandr@ujn.edu.cn*

ABSTRACT

The hydrodynamic coefficient of an underwater manipulator varies with changes in posture and flow field, presenting significant challenges for precise control and localization. This study, conducted numerical simulations to investigate the patterns of variation in flow field and hydrodynamic coefficients. Results showed that hydrodynamic performance remained consistent when the posture of the manipulator was either axisymmetric or origin-symmetric. Upon rotation, axial flow extended across the entire downstream surface, and the Karman vortex street entirely eliminated. Pressure coefficients on the back pressure surface of the manipulator increased with the Reynolds number within the range of $6\times10^3 \leq Re \leq 3\times10^4$, while the pressure coefficient on the upstream surface remained unchanged. Within this range, drag coefficients for the upper and lower arms decreased by 27.4% and 23.9%, respectively. The hydrodynamic performance of the lower arm was independent of the upper arm's posture, with a maximum drag coefficient of 1.48 achieved at $\alpha = -90°$. As the posture angle of the manipulator varied from 30° to 60°, the pressure coefficient on the upstream surface decreased from 0.75 to 0.25.

Article History

Received January 17, 2024
Revised March 3, 2024
Accepted March 19, 2024
Available online July 2, 2024

Keywords:

Underwater manipulator
Pressure coefficient
Drag coefficient
Free ends
Flow structure

1. INTRODUCTION

The advancement of ocean exploration technologies, has led to widespread use of underwater manipulators for tasks such as underwater collection, ocean exploration, and equipment maintenance (Wu et al., 2019; Xu et al., 2021). Unlike their land-based counterparts, underwater manipulators must contend with their own gravity and payload, as well as hydrodynamic forces and moments from the aquatic environment. These factors significantly affect operation performance, especially in terms of motion control, leading to potential inaccuracies in operating precision (Liu et al., 2022). Accurate determination of hydrodynamic coefficients and flow field characteristics is crucial for enhancing the performance of underwater manipulators (Wang et al., 2021).

Numerous scholars have investigated the underwater motion of manipulators, noting the significant impact fluid dynamic (Carlucho et al., 2021). Among various physical aspects, the variation in hydrodynamic coefficients has emerged as a critical area of study. Due to the development stage of viscous wave theory, hydrodynamic coefficients have often been selected based on empirical values derived from potential flow theory. (Avila et al., 2008; Suzuki et al., 2013). Viscous hydrodynamics, plays a crucial role in controlling underwater manipulators (Zhang et al., 2019). For in-depth analysis, researchers have modeled underwater manipulators as consisting of cylindrical connecting rods, discovering that drag force depends solely on the velocity component perpendicular to the cylinder's axis, with a constant drag coefficient (Schjølberg & Egeland 1995). Kolodziejczyk et al. (2023) assessed the transient hydrodynamic coefficient by examining a rotating underwater manipulator, revealing that the drag and added inertia coefficients depend on time and shape.

However, fluid flow around an underwater manipulator is considerably more complex than around a finitely long cylinder. McLain and Rock (1998) conducted tests on a cylindrical manipulator arm with a single degree of freedom in rotation, demonstrating variable drag coefficients with motion. Tsukrov et al. (2011) showed that changes in the Reynolds number affect hydrodynamic coefficient. Kolodziejczyk (2015, 2016) calculated the joint moments of an underwater manipulator in eight different postures using computational fluid dynamics

Nomenclature

A	inclined posture cross section
C_D	drag coefficient
C_L	lift coefficient
C_P	pressure coefficient
D	diameter
D_ω	orthogonal divergence term
F_D	lift force
F_L	drag force
G_k	turbulent kinetic energy
G_ω	ω equation
L	length of arm
P	dynamic pressure
Re	Reynolds number
t	time
U_i	x_i-direction component of the flow field velocity
U_j	x_j-direction component of the flow field velocity
U	fluid velocity
v	dynamic viscosity coefficient
x_i	horizontal directions
x_j	horizontal directions
Y_k	divergence of k model
Y_ω	divergence of ω model
y	distance to the next surface
Z	vertical posture cross section

Greek letters

α	manipulator offset angle
β	angle of attack
Γ_k	effective diffusion terms of k
Γ_ω	effective diffusion terms of ω
δ_{ij}	Kronecker delta function
μ	hydrodynamic viscosity
μ_t	turbulent viscosity
ρ	fluid density
σ_k	turbulent Prandtl numbers for k
σ_ω	turbulent Prandtl numbers for ω
ω	vorticity

(CFD), finding variance in joint moments and hydrodynamic depending on fluid position and manipulator orientation. Using CFD simulations, transient dynamic loads and coefficients for a single degree of freedom manipulator were obtained, employing dynamic mesh techniques to simulate arm movements under varying kinematic conditions (Kolodziejczyk, 2018). Cheng et al. (2022) examined the effects of cross-section shape and spacing on the hydrodynamic performance, with two-dimensional numerical calculations indicating significant reductions in lift and drag coefficients for elliptical versus circular sections. Duan et al. (2023a) explored the hydrodynamic performance of a single-arm manipulator, assessing the influence of velocities, postures, and inflow directions on hydrodynamic coefficients and flow characteristics. Stability was noted when the elliptical section faced upstream (Duan et al. 2023b), but variations in vortex shedding and hydrodynamic coefficients at the cross-section, joints, and free end of the manipulator were not addressed.

In addition to the effects of posture and Reynolds number, lateral and end flow fields exist for underwater manipulators modeled as combinations of finite length cylinders (Hölscher & Niemann 1996; Cakir et al., 2015). Chen et al. (2009) found that the drag coefficient from a three-dimensional cylindrical model was smaller than that from a two-dimensional model by examining an infinitely long cylindrical model. Roh and Park (2003), using a smoke-laser sheet, visualized flow in a finite cylinder and observed vortex flow along the free end faces, characterizing the flow on the free end surface topologically. Axial flow occurs when fluid moves through the free end of a finite length column. Sumner and Heseltine (2008) experimentally explored the vortex structure near the free end of a cylinder at a Reynolds number of 6×10^4, noting strong downwash velocities behind the cylinder below the free end, which weakened towards the bottom. Gao et al. (2018) analyzed the hydrodynamic characteristics of a finite-length cylinder with two free ends through numerical calculations, finding that flow pattern and turbulence structure vary with aspect ratio and Reynolds number.

These studies indicate that both posture and Reynolds number significantly influence the hydrodynamic performance of underwater manipulators. Additionally, the free end also impacts manipulator control. Therefore, it is crucial to study the hydrodynamic coefficients and flow field characteristics of the underwater manipulator. This research, considering the hydrological environment of the Shandong Peninsula sea area, discusses the flow field structure, pressure distribution, and drag coefficients of underwater manipulators at various postures and Reynolds numbers. The findings aim to provide a more accurate theoretical foundation for constructing the hydrodynamic model of the manipulator.

The remainder of the paper is organized as follows: the model building is introduced firstly, including the mathematical model, governing equations, turbulence model, parameter setting, mesh dependence, and numerical verification in this work. Results and discussion are then devoted to study the effects of Reynolds number and posture on the hydrodynamic performance. Finally, some conclusions are summarized in the Conclusion section.

2. MODEL BUILDING

2.1 Mathematical Model

The geometry of the fluid domain and boundary condition is depicted in Fig. 1. In this figure, the D represents the diameter of the underwater manipulator, with L_1 and L_2 denoting the lengths of the upper and lower arms, respectively, both being ten times the diameter. The center of the lower arm is positioned $10D$ downstream from the inlet and $30D$ from the outlet, with the distance between the front and back wall surfaces and the manipulator set at $8D$, and the gap between the upper wall surface and the manipulator at $10D$.

Figure 2 displays the posture grip of the underwater manipulator. The vertical posture is defined as the initial posture, when the posture pinch angle $\alpha = 0°$. Rotation to the right and left is positive and negative, respectively.

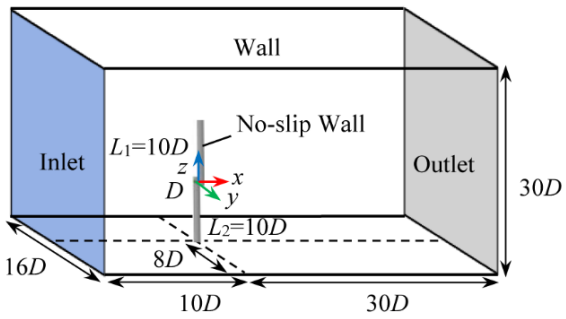

Fig. 1 Geometry and boundary condition of the calculation domain

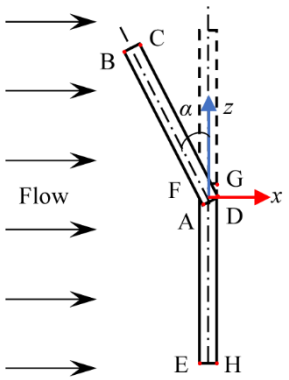

Fig. 2 Schematic diagram of underwater manipulator posture

Moreover, A~H represented the vertices of the longitudinal section.

2.2 Governing Equations and Turbulence Model

This study models the flow around underwater manipulators using the Reynolds-averaged Navier-Stokes (RANS) equations (Yu & Thé 2016). To simplify, the flow problem is transformed into an internal flow problem by establishing an appropriate virtual boundary around the manipulator. The RANS equations are then solved within space enclosed by this boundary. When considering viscous, incompressible fluid as the medium, the RANS equation can be expressed as follows:

$$\frac{\partial U_i}{\partial x_i} = 0 \tag{1}$$

$$\frac{\partial U_i}{\partial t} + U_j \frac{\partial U_i}{\partial x_j} = -\frac{1}{\rho}\frac{\partial P}{\partial x_i} + \upsilon \frac{\partial^2 U_i}{\partial x_j^2} - \frac{\partial \overline{u_i u_j}}{\partial x_j} \tag{2}$$

where, ρ, P and ν represent fluid density, dynamic pressure, and dynamic viscosity coefficient, respectively. x_i and y_i denote the horizontal and vertical directions. U_i and U_j are the corresponding mean velocity components. $\overline{u_i u_j}$ is the Reynolds stress component and using the Boussinesq approximation is

$$-\overline{u_i u_j} = \mu_t \left(\frac{\partial U_i}{\partial x_j} + \frac{\partial U_j}{\partial x_i} \right) - \frac{2}{3}\delta_{ij} G_k \tag{3}$$

where, μ_t stands for the turbulent viscosity, δ_{ij} is the Kronecker delta function, and G_k is turbulent kinetic energy. The equations are dimensionless with appropriate velocity and length scales,

$$\frac{\partial U_i}{\partial t} + U_j \frac{\partial U_i}{\partial x_j} = -\frac{\partial P}{\partial x_i} + \frac{1}{Re}\frac{\partial^2 U_i}{\partial x_j^2} - \frac{\partial \overline{u_i u_j}}{\partial x_j} \tag{4}$$

Re is the Reynolds number, which a dimensionless number utilized to characterize fluid flow.

$$Re = \frac{\rho U D}{\mu} \tag{5}$$

where, U represents fluid velocity, μ is the hydrodynamic viscosity.

Compared with other turbulence model, the SST k-ω turbulence model considers the transmission of turbulent shear stress in the definition of turbulent viscosity (Menter, 1993). Herein, the turbulence model includes the equations of the turbulent kinetic energy(k) and the specific dissipation rate(ω) as follows:

$$\frac{\partial(\rho k)}{\partial t} + \frac{\partial(\rho k U_i)}{\partial x_i} = \frac{\partial(\Gamma_k \dfrac{\partial k}{\partial x_j})}{\partial x_j} + G_k - Y_k + S_k \tag{6}$$

$$\frac{\partial(\rho \omega)}{\partial t} + \frac{\partial(\rho \omega U_i)}{\partial x_i} = \frac{\partial(\Gamma_\omega \dfrac{\partial \omega}{\partial x_j})}{\partial x_j} + G_\omega - Y_\omega + D_\omega + S_\omega \tag{7}$$

where, G_k represents the turbulent kinetic energy due to the average velocity gradients. G_ω denotes the generation of ω. Γ_k and Γ_ω are the effective diffusivity of k and ω, respectively. Y_k and Y_ω denote the dissipation of k and ω due to turbulence. D_ω stands for the cross-diffusion term. S_k and S_ω are user defined source terms.

$$\Gamma_k = \mu + \frac{\mu_t}{\sigma_k} \tag{8}$$

$$\Gamma_\omega = \mu + \frac{\mu_t}{\sigma_\omega} \tag{9}$$

where σ_k and σ_ω represent the turbulent Prandtl numbers for k and ω, respectively.

$$\sigma_k = \frac{1}{F_1/\sigma_{k,1} + (1-F_1)/\sigma_{k,2}} \tag{10}$$

$$\sigma_\omega = \frac{1}{F_1/\sigma_{\omega,1} + (1-F_1)/\sigma_{\omega,2}} \tag{11}$$

where, the blending function F_1 is given by

$$F_1 = \tanh\left(\Phi_1^4\right) \tag{12}$$

$$\Phi_2 = \min\left[\max\left(\frac{\sqrt{k}}{0.09\omega y}, \frac{500\mu}{\rho y^2 \omega} \right), \frac{4\rho k}{\sigma_{\omega,2} D_\omega^+ y^2} \right] \tag{13}$$

$$D_\omega^+ = \max\left[2\rho \frac{1}{\sigma_{\omega,2}} \frac{1}{\omega} \frac{\partial k}{\partial x_j} \frac{\partial \omega}{\partial x_j}, 10^{-10} \right] \tag{14}$$

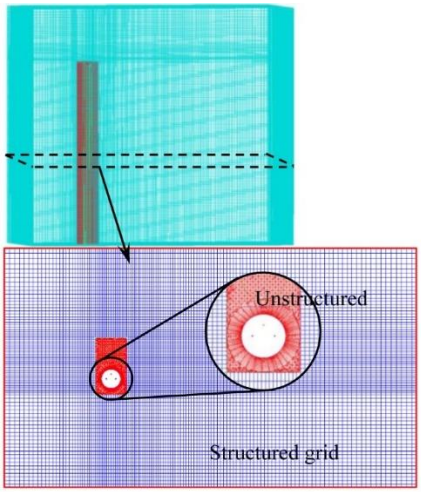

Fig. 3 Hybrid meshing result

where y is the distance to the next surface. The D_{ω}^{+} represents the positive portion of the cross-diffusion term. The turbulent viscosity is calculated as follows:

$$\mu_t = \frac{\rho k}{\omega} \frac{1}{\max\left[\frac{1}{\alpha^*}, \frac{SF_2}{a_1 \omega}\right]} \tag{15}$$

where S represents the strain rate magnitude. a^* represents damps the turbulent viscosity, in the high Reynolds number form of the k-ω model, a^*=1. F_2 is given by

$$F_2 = \tanh\left(\Phi_2^2\right) \tag{16}$$

$$\Phi_2 = \max\left[2\frac{\sqrt{k}}{0.09\omega y}, \frac{500\mu}{\rho y^2 \omega}\right] \tag{17}$$

2.3 Parameter Setting and Mesh Dependence

A velocity inlet was applied at the inlet of the domain, and a pressure outlet was utilized at the exit, assuming zero gauge pressure at the outlet plane. No-slip boundary conditions were applied to the walls on both sides. Reflecting the hydrological environment of the Shandong Peninsula sea area, the study investigated the variation in within Reynold numbers from 6.0×10^3 to 3.0×10^4, corresponding to fluid velocities of 0.2 to 1.0 m/s. Additionally, flow field characteristics of different postures were examined in a steady flow environment at Re = 1.8×10^4, with water as the fluid medium.

The structured meshing of the fluid domain faced challenges due to the tangential surfaces present in the underwater manipulator model. To balance mesh quantity and result accuracy, a hybrid mesh approach was employed for the computational domain. Figure 3 displays the three-dimensional schematic and horizontal cross-section diagram of the hybrid mesh. Using the vertical posture model as an example, areas near the manipulator were divided using an unstructured grid, while other areas utilized a structured mesh.

To characterize the hydrodynamic performance, the drag coefficient C_D, lift coefficient C_L, and pressure coefficient C_P were defined as,

$$C_D = \frac{F_D}{\frac{1}{2}\rho U^2 D} \tag{18}$$

$$C_L = \frac{F_L}{\frac{1}{2}\rho U^2 D} \tag{19}$$

$$C_P = \frac{p_i - p_\infty}{\frac{1}{2}\rho U^2} \tag{20}$$

where, D is the diameter of the underwater manipulator, F_D and F_L represents the drag and lift forces acting the cross-section of the manipulator. p_i is the pressure at a certain point on the surface of the manipulator, and p_∞ is the far-field static pressure, namely the environmental pressure.

To determine optimal meshing parameters, three mesh groups with varying numbers of boundary layers were analyzed, calculating the drag coefficients (C_D) and the lift coefficients (C_L) of the lower arm. The findings, listed in Table 1, show that both coefficients varied with the number of meshes. The maximum variations observed for C_D and C_L were 4.1% and 4.3%, respectively. Thus, to optimize computational resources and accuracy, the study selected the mesh configuration corresponding to Mesh2 for subsequent simulations.

2.4 Numerical Approach Validation

The study modeled underwater manipulator model as a combination of finite length columns, necessitating a comparison of results with those concerning a finite length column. Table 2 presents data validation the numerical method, with selected domain and parameter settings aligning with those reported in the literature. The calculated drag coefficient (C_D) was compared against existing three-dimensional data, revealing maximum and minimum errors of 4.8% and 0.7%, respectively. Based on the comparison results of finite length column, the errors were within an acceptable range. It observed that the turbulence model has stable performance in solving the problem of the finite-length cylindrical flow field. Thus, the turbulence model was chosen to be applied in this study.

Table 1 Grid independence verification

Group	Layer	Elements	C_D	Relative error	C_L	Relative error
1	10	1273991	0.721	——	0.0682	——
2	15	1427728	0.714	0.97%	0.0704	3.2%
3	20	1682025	0.751	4.1%	0.0711	4.3%

Table 2 Numerical method validation

Re	*L/B*	C_D	Relative error	Data source
3900	π	0.782	——	Wang et al. (2018)
3900	π	0.744	4.8%	*k-ω* SST
13000	10	0.7	——	Okamoto nd Yagita (1973)
13000	10	0.705	0.7%	*k-ω* SST
30000	10	0.76	——	Liang et al. (2021)
30000	10	0.781	2.8%	*k-ω* SST

3. RESULTS AND DISCUSSION

3.1 Flow Field Structure of Cross-Sections at Different Positions

Previous studies have shown that axial flow occurs when fluid passes through the free end of a finite-length column, resulting in variations in pressure and drag coefficients across different cross-sections of the column (Zdravkovich et al., 1989; Park & Lee 2004). This study aimed to explore how the C_P and C_D vary along the axial direction of an underwater manipulator, examining cross-sections in various positions while the manipulator is in a vertical posture.

Figure 4 illustrates the velocity contours of the longitudinal cross-section at both arms and the joint for Re=1.8×10^4. In conjunction with Fig. 5, it is observed that the reflux zone near the upper arm's top gradually increases from top to bottom, reaching its maximum at cross-section Z_2 (H_2/L_1=0.7) and then remaining constant. Thus, the axial flow at the end face influences the wake region created by the lateral bypass, and vice versa. It was also the reason for the limited axial flow distance of the fluid at the end face (Sumner, 2013).

As depicted in Fig. 4(b), the low velocity zone behind the joint is longer than at other locations due to the joint structure impending fluid flow, requiring a longer distance for velocity recovery. Figure 4(a) and 4(c) suggest that the bottom of the upper arm and the area near the top of the lower arm also exhibit an increasing low velocity region, indicating the presence of axial end flow at these locations. This finding aligns with Kawamura et al. (2002), who noted that the vortex structure at both locations is closely related to the morphology of the free surface, though it overlaps with the wake field behind the joint and is less pronounced than the flow field near the upper arm's top.

Figure 5 illustrates the vortex contour diagram of the horizontal cross-section at different height positions of the upper arm at Re = 1.8×10^4. The wake flow field shows significant variation across different horizontal cross-sections. Near the free end of the underwater manipulator, the tail flow field lacks notable vortex shedding alternation. However, significant vortex shedding alternation is observed in the wake flow field at the middle position of the upper arm, suggesting that the axial flow at the manipulator's end face in a vertical posture impacts vortex shedding, albeit within a limited range (Pattenden et al., 2007). Similar to the tail flow field at various positions of the upper arm, vortex shedding near the top of the lower arm was similarly disrupted due to the combined effects of axial flow from the end face and the joint structure. As the position moved down, the effect of the end face on the axial flow diminished until its disappeared. Consequently, clear alternating vortex shedding persisted in the middle and lower sections of the lower arm, with the vortex at cross-section Z_1 significantly diminished by its proximity to the wall. The vortex in the tail flow field of cross-section Z_1 disappeared earlier compared to the cross-section at other positions, and Park & Lee (2000) similarly observed that the vortex shedding disappeared to be closely related the free end.

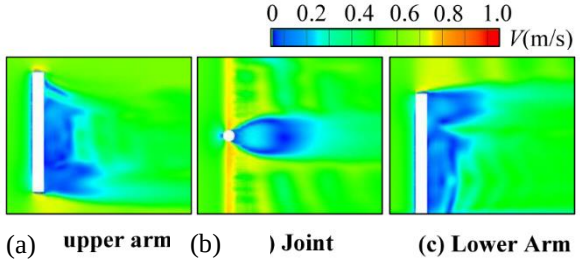

Fig. 4 Velocity contours at different positions of the longitudinal section

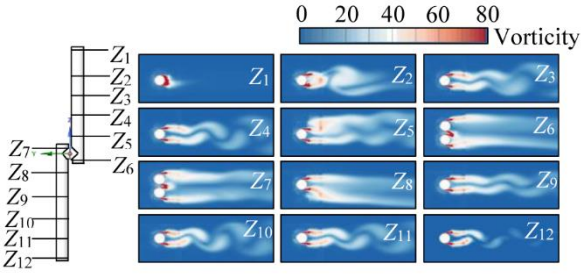

Fig. 5 Vorticity contours of different horizontal cross-sections

3.2 Pressure Coefficient for Cross-Sections at Different Positions

Figures 6 and 7 illustrate the temporal and spatial variations of the C_P across different cross-sections in a vertical posture at Re = 1.8×10^4. The angle of the outer circle in these figures represents the counterclockwise direction from the rear on the horizontal axis of the section. The pressure coefficient curves in the regions of cross-sections Z_2 to Z_5 and Z_8 to Z_{12} essentially overlapped, indicating some locations were minimally affected by axial and tail flows near the joint, exhibiting a consistent circumferential pressure coefficient distribution pattern. The maximum circumferential pressure coefficient for these sections occurred directly opposite to the incoming

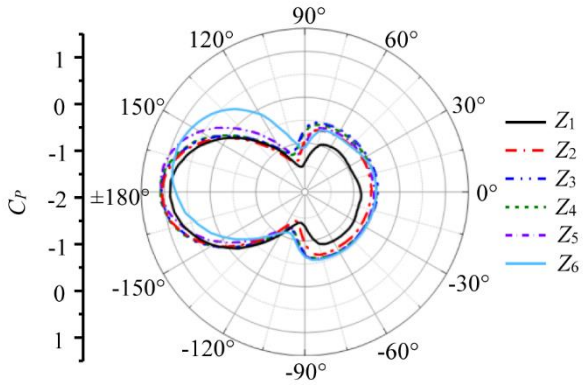

Fig. 6 Pressure coefficient of upper arm at different horizontal cross-sections

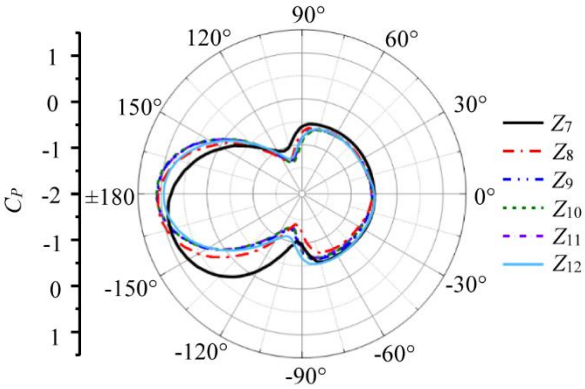

Fig. 7 Pressure coefficient of lower arm at different horizontal cross-sections

flow (θ = ±180°), with values around 1.0. As the flow of fluid to both sides of the column, C_P decreased rapidly and reached a minimum value of about −1.5 at θ = ±110°. Subsequently, the pressure coefficients gradually flatten out towards the downstream surface. The trend of this circumferential distribution of pressure coefficients was consistent with that reported by Gao et al. (2021). Conversely, in Fig. 8, the pressure coefficient at the Z_1 cross-section of the downstream surface of the upper arm was notably lower than at other positions, decreasing as the cross-section approached the free end due to axial flow through the end.

In Figs. 6 and 7, the maximum values for sections Z_6 and Z_7 did not align opposite the incoming flow but shifted toward the joint. Figure 8 illustrates that the high-pressure zone gradually moves toward the joint as it approached the joint position. This shift resulted from the narrow gap between the upper and lower arms at the joint, where fluid acceleration occurred due to the sudden narrowing, affecting the positioning of the pressure coefficient values. At last, the position of the minimum value in these two cross-sections varied from θ = ±110° to θ = 105° and θ = −95° (Zhang et al., 2021).

Figure 9 depicts the pressure coefficients distribution of the longitudinal cross-section at Re = 1.8×10⁴. The location of the longitudinal cross-section is the semi-profile of the upper arm and lower arm. Figure 9, with the horizontal coordinate representing the spreading distance (L), shows the spreading length of the upper arm as

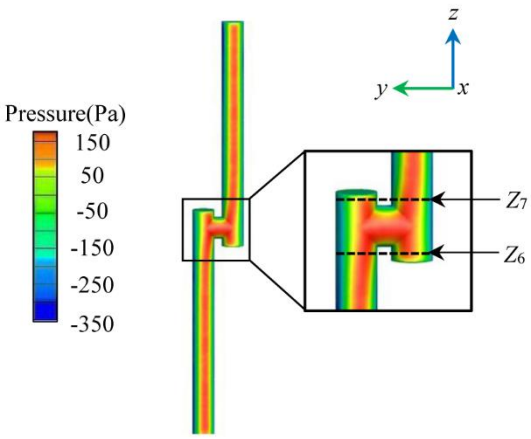

Fig. 8 Pressure contour of the upstream face

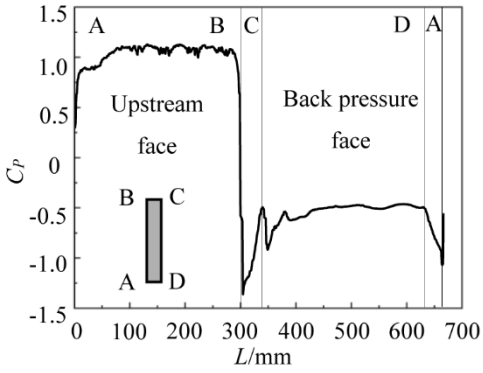

(a) Upper Arm

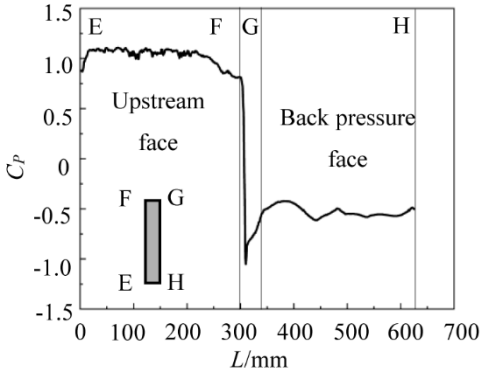

(b) Lower Arm

Fig. 9 Axial pressure coefficient of longitudinal cross-sections

660mm and the lower arm's as 630mm, with A~H making different vertices of the longitudinal section. The maximum pressure coefficient (C_{Pmax}) appeared on the upstream surface, around 1.0. Near the end face, the pressure coefficient decreased, reaching its minimum at points B and F, with the upper arm's minimum pressure coefficient (C_{Pmin}) at approximately −1.5, and the lower arm's C_{Pmin} at approximately −1.0.

From Fig. 9, the pressure coefficient on the upstream face was positive, while those on the downstream and end faces were negative. The upstream face experienced direct impact from fluid flow, whereas the downstream face was

within the reflux zone, characterized by slower fluid flow rates. Furthermore, it was observed that pressure coefficients changed abruptly at points where the shape changed significantly, such as at endpoints B, C, and F. This change was attributed to the removal of blockage at these points, resulting in increased fluid velocity and decreased pressure nearby.

In the prior section, the distribution of circumferential pressure coefficients remained consistent across all horizontal cross-sections, except those near the tops and joint. Hence, the circumferential pressure coefficients at different Reynolds numbers will be discussed and analyzed next, taking cross-sections Z_3 and Z_9 as examples.

Figures 10 and 11 show the circumferential pressure coefficient curves for cross-sections Z_3 (H_3/L_1=0.5) and Z_9 (H_9/L_2=0.5) at varying Reynolds numbers. The pressure coefficient curves of the upstream face at different Reynolds numbers varied little. It was noted that pressure coefficients increased with the Reynolds number on the downstream surface, leading to a reduced pressure differential between the front and rear of the underwater manipulator. Additionally, the minimum pressure coefficient decreased as the Reynolds number increased. As the Reynolds number increased from 6.0×10^3 to 3.0×10^4, the minimum value of the pressure coefficient raised from −0.57 to −1.4. In addition, the location where the minimum value of the circumferential pressure coefficient also moved backward as the Reynolds number enhanced. Namely, an increase in Reynolds number causes the vortex shedding to shift rearward.

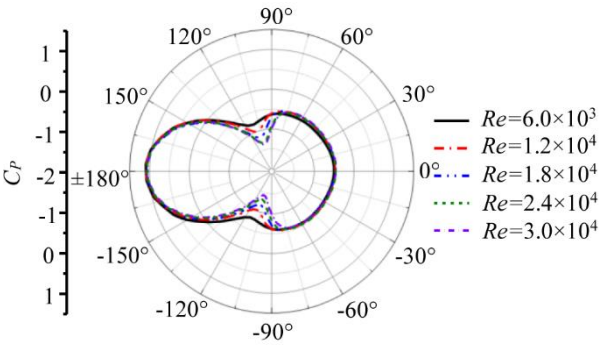

Fig. 10 Pressure coefficient of the Z_3 cross-section in the upper arm at different Reynolds numbers

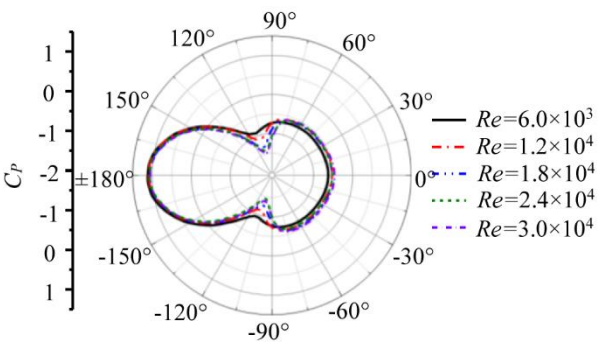

Fig. 11 Pressure coefficient of the Z_9 cross-section in the lower arm at different Reynolds numbers

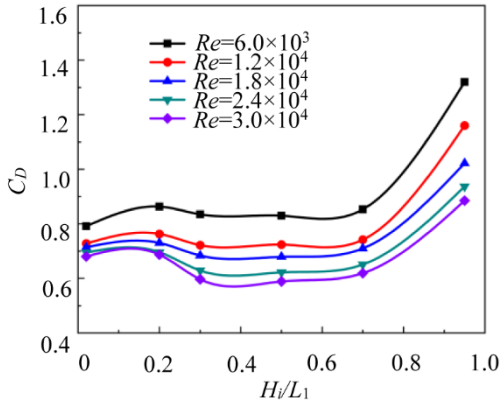

(a) Upper Arm

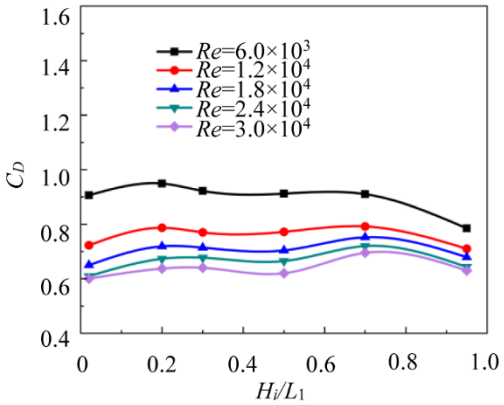

(b) Lower Arm

Fig. 12 Drag coefficients of each horizontal cross-section at different Reynolds numbers

Analyzing the C_P across different cross-sections and longitudinal sections of the underwater manipulator revealed the C_P distribution on the surface of the manipulator (Jung & Chung 2012). Investigating this pressure distribution under steady flow conditions allows for a deeper understanding of flow field characteristics, such as vortex shedding. Unlike steady flow, near-wall flow states are more complex in unsteady conditions, with acceleration significantly affecting the coefficient (He et al., 2014; Kharghani & Pasandidehfard, 2022). Generally, the C_P in unsteady flow exhibits periodic variations. A rotating vortex forms around the manipulator cylinder, leading to a brief decrease in C_P as the vortex moves to the tail of the cylinder. The maximum pressure coefficient typically occurs at the leading or trailing edge of the cylinder, due to strong interactions between static and dynamic pressures at these locations (He et al., 2013; PasandidehFard & Naeimirad, 2022).

3.3 Drag Coefficient for Different Horizontal Sections

Figure 12 illustrates the drag coefficients for each horizontal cross-section of the upper and lower arms at varying Reynolds numbers. From Fig. 12(a), the drag coefficient varied with the increase of cross-section height. A significantly increase in drag coefficient was observed near the top of the upper arm, attributed to climbing fluid flow at the front and axial flow at the rear. Between cross-sections Z_2 and Z_4, the drag coefficient varied less, indication minimal impact from the axial flow of the top fluid in this zone. Near the bottom of the upper

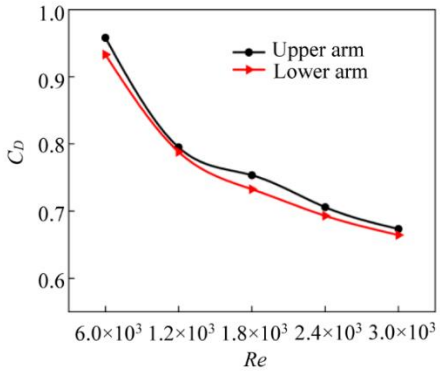

Fig. 13 Drag coefficients of the whole upper and lower arms at different Reynolds numbers

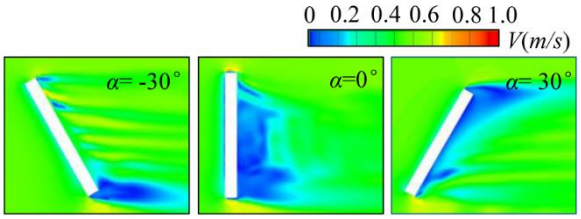

Fig. 14 Velocity contour diagram of the upper arm near flow field at different postures

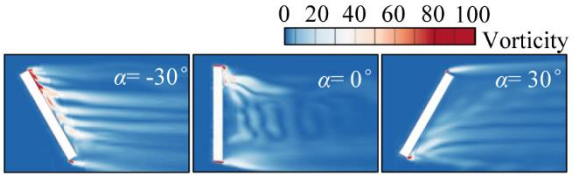

Fig. 15 Vorticity contour diagram of the upper arm near flow field at different postures

arm, the increase in drag coefficient was less pronounced than near the top, as the joint structure diminished the effect of the axial flow at the bottom. From Fig. 12(b), with the increase of cross-section height, the drag coefficient varied little. The drag coefficient experienced an increase followed by a decrease near the top due, influenced by the connection structure and axial flow of fluid. The drag coefficient at the bottom position of the lower arm was also reduced, probably due to the proximity to the fluid domain wall (Alzabari et al., 2023). Comparison of drag coefficients at different Reynolds numbers revealed a decrease in drag coefficients across all horizontal sections as Reynolds numbers increased. This variation was not limited to a few individual horizontal sections but applied to all sections of the underwater manipulator. The same trend of this variation in the drag coefficient was observed in the study of finite length cylinders by Gao et al. (2018).

Figure 13 displays the drag coefficients of the entire upper and lower arms at various Reynolds numbers. When the Reynolds number raised from 6.0×10^3 to 3.0×10^4, the drag coefficients of the upper and lower arms reduced by 27.4% and 23.9%. The drag coefficients for both arms followed the same trend, decreasing with an increase in Reynolds number. Notably, the drag coefficients of the upper arm were slightly higher than those of the lower arm, likely due to the more pronounced effects of climbing fluid flow at the front and downwash flow at the rear on the upper arm.

Meanwhile, the drag coefficient of the overall upper arm was 0.75. The drag coefficient for the entire upper arm was close to the average value of the drag coefficients for each cross-section at $Re = 1.8\times10^4$. The drag coefficient for the whole lower arm was 0.73, aligning not only with the average value of the drag coefficients for each cross-section of the lower arm but also with the drag coefficients of the middle and lower parts of the lower arm. In regions unaffected by axial fluid flow, the drag coefficient of a cross-section resembled that of the whole.

3.4 Flow Field Structure of Underwater Manipulator in Different Postures

This section examines how changes in the posture of the manipulator the flow field structure by comparing the near-flow fields in various postures. Figure 14 shows velocity contour diagrams for the upper arm at offset angles α of −30°, 0°, and 30°. Rotation of the upper arm significantly expanded the influence range of axial flow compared to the vertical posture. At $\alpha = -30°$, fluid flowed axially from the top to the bottom end, leaving the downstream surface to merge with the bottom fluid, indicating that manipulator rotation increased the axial flow distance of the end fluid. Finally, a wake flow in the blue region was formed behind the bottom end. Nevertheless, in the vertical posture, the fluid has a limited axial flow distance and did not flow the entire arm section as in the -30° and 30° postures. This suggested that the rotation of the underwater manipulator increased the axial flow distance of the end fluid. This phenomenon, also observed by Wang et al. (2020) in studies inclined cylinder wake, highlights the impact of posture on flow dynamics.

Vorticity contour plots for the upper arm at offset angles α of −30°, 0°, and 30° are presented in Fig. 15. These plots reveal the absence of a vortex shedding zone behind the upper arm at offset angles of -30° and 30°, unlike at α=0°. The rotation induced axial fluid flow along the upper arm, disrupting vortex formation across the entire arm section. Notably, fluid shedding from the surface during the axial flow formed a band vortex behind the manipulator, differing from the alternately shed Karman vortex typically seen alongside a column. This variation results from the axial flow being influenced by later fluid motion.

To further investigate the impact of axial flow on lateral vortex shedding, vorticity contour plots at various horizontal cross-sections of the upper arm at a 30° posture angle were analyzed. To distinguish from the vertical posture horizontal cross-section in the previous portion, the cross-section of this section was selected as shown in Fig. 16. A_1~A_6 were the codes for different horizontal cross-sections.

Figure 17 displays the vorticity contours at different horizontal cross-sections with the upper arm rotated 30° to the right. There was no vortex shedding on both sides of each horizontal cross-section although there were high

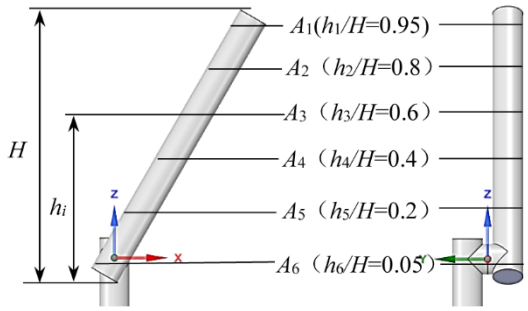

Fig. 16 Position of the horizontal cross-section on the tilted upper arm

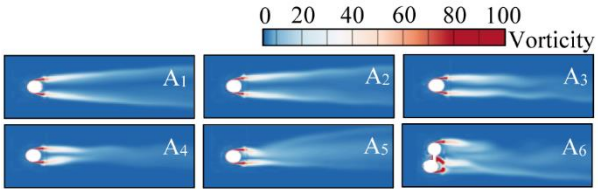

Fig. 17 Vorticity contours of different horizontal cross-sections in the upper arm

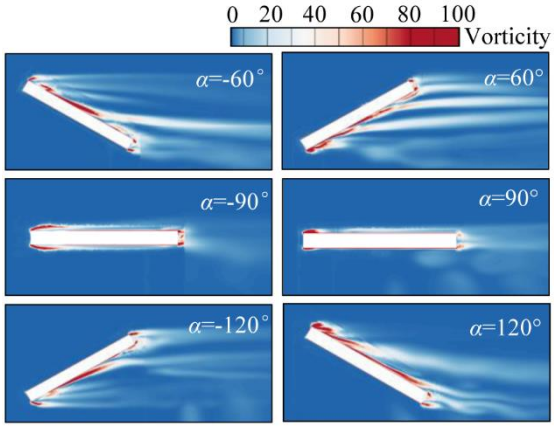

Fig. 18 Vorticity contours of the longitudinal cross-section on the upper arm at different postures

vorticity areas. In this posture, the axial flow of the fluid influenced the entire arm segment. This rotation prevented the formation of a Karman vortex street, a phenomenon also noted by Hu et al (2016). Figure 18 shows vortex contours in the longitudinal section of the upper arm at posture angles α of −120°, −90°, −60°, 60°, 90°, and 120°, corresponding to the attack angles β of 150°, 90°, 30°, 150°, 90°, and 30°, respectively. In Fig. 18, the underwater manipulator was in a similar flow field environment when its posture was either axisymmetric or origin-symmetric. Similar vortex variations occurred behind the manipulator at posture angles α of −60° and 120°, with identical band vortices forming at the rear end of the bottom.

From the analysis, it evident that underwater manipulators exhibit similar flow field environments when their postures are either axisymmetric or origin-symmetric. Specifically, when the α of two manipulators are either opposite to each other or their absolute values sum to 180°, the manipulators display similar flow field environments. Similarly, for β, similar flow field

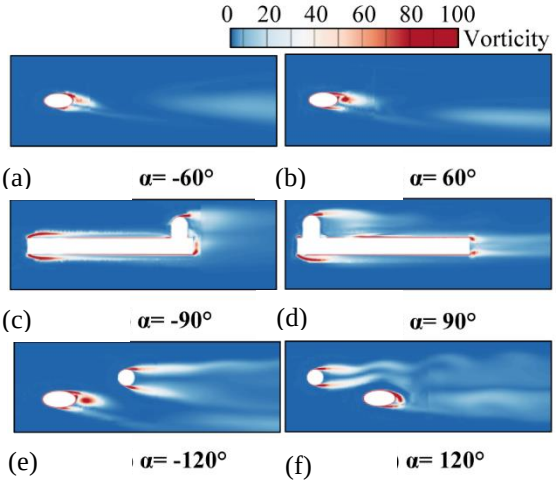

Fig. 19 Vorticity contours at the cross-section A_3 of the upper arm in different postures

environments are observed if the incoming flow attack angles corresponding to the two postures are equal or their sum equals 180°.

To more intuitively investigate the flow field generated by lateral winding around the upper arm in various postures, vorticity contours of the upper arm's cross-section A_3 (h_3/H = 0.6) for posture angles of −120°, −90°, −60°, 60°, 90°, and 120° were compared and analyzed, as illustrated in Fig. 19. The upper arm of the underwater manipulator had the same near-flow field environment when they were either axisymmetric or origin-symmetric. Such as, the vorticity distribution at the cross-section A_3 (h_3/H=0.6) of the upper arm was the same for the posture angle α= 60° and α= −120°. When the upper arm was positioned in front of the lower arm, the wake from the upper arm hindered vortex shedding in the wake of the lower arm. As shown in Fig. 19(f), with the upper arm at an angle α = 120° and positioned behind the lower arm, the latter was no longer influenced by the wake field of the upper arm. Thereby, there was still vortex shedding in cross-section A_3 of the lower arm. Meanwhile, the vorticity intensity in the vicinity of the upper arm was weakened due to the lower arm wake.

Figure 20 demonstrates the vorticity contours of the lower arm longitudinal profiles for the upper arm at

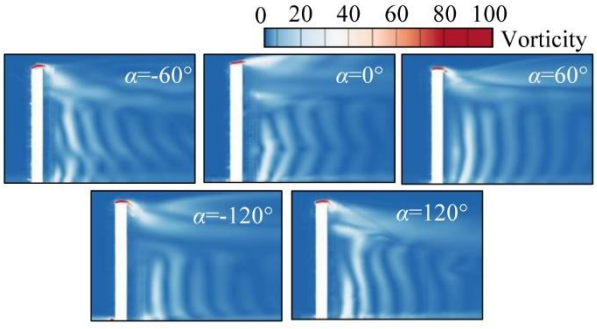

Fig. 20 Vorticity contours of the lower arm longitudinal profile when the upper arm was in different postures

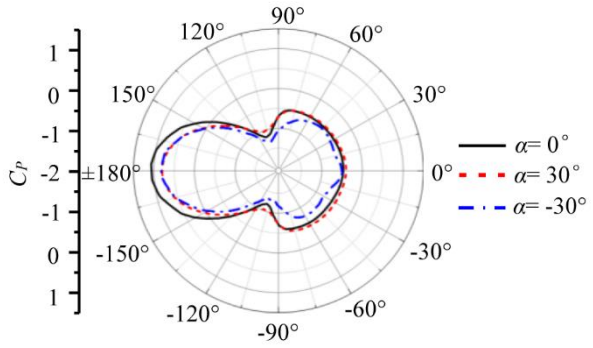

Fig. 21 Pressure coefficient of the cross-section A_3 in the upper arm at different postures

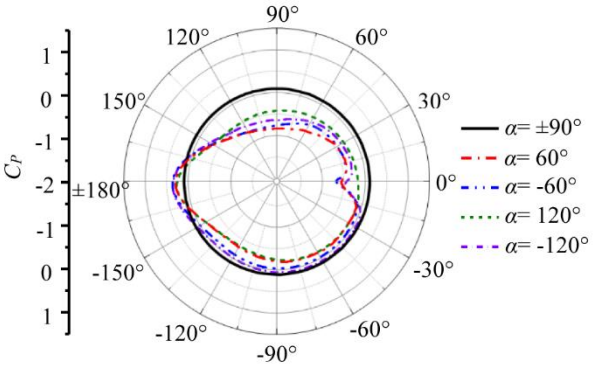

Fig. 22 Pressure coefficient curves at the cross-section A_3 of the upper arm in the symmetric posture

different postures. The change in the posture of the upper arm had minimal impact on the extent of the vortex-free region near the top of the lower arm. However, as previously discussed, the hydrodynamics of the entire lower arm are primarily influenced by the environment at its middle and lower parts. Therefore, the effect of the upper arm posture changes on the lower arm hydrodynamics was limited.

3.5 Pressure Coefficient in Different Postures

Figure 21 presents the circumferential pressure coefficient curves at cross-section A_3 (h_3/H=0.6) of the upper arm for posture of −30°, 0°, and 30°, respectively. The comparison showed that the rotation of the upper arm decreased the pressure coefficient on the upstream surface (Franzini et al., 2009). Additionally, the pressure coefficient of the downstream surface also decreased due to the axial flow. The magnitude of reduction was smaller than that observed on the upstream surface, leading to a decreased difference in pressure coefficients between the front and rear of the underwater manipulator. Therefore, the drag coefficient of the underwater manipulator was decreased accordingly.

Figure 22 represents the circumferential pressure coefficient curves at the cross-section A_3 (h_3/H=0.6) of the upper arm for symmetrical postures, where the angle α= ±90° is the vertical cross-section. It is inferred that the circumferential pressure coefficient is uniformly distributed when the upper arm adopts a horizontal posture (α= ±90°), indicating no impact on the side of the column due to the incoming flow attack angle (β) being 0°. Additionally, the circumferential pressure coefficient curves at the cross-section did not align perfectly with those of their corresponding symmetrical postures (α= 60° and α= 120°) when the posture angles were α= −60° and α= −120°. The difference is that the flow field at the cross-section was affected by the flow field at the top of the lower arm. It was larger on the upper side of the upper arm. Therefore, excluding the influence of the flow field at the top of the lower arm, the distribution of circumferential pressure coefficients at the same horizontal position of the cross-section remains consistent when the upper arm's postures are axisymmetric or origin-symmetric.

Figures 23 to 26 depict the axial pressure coefficient curves along the longitudinal profile of the upper arm in various postures. It was observed that the maximum axial pressure coefficient typically occurred near the intersection of the long and short sides of the upstream surface, exemplified by point B in Fig. 23(a) and point C in Fig. 26(a). Conversely, the minimum axial pressure coefficient was found near the intersection of the long and short sides on the downstream surface, as shown at point D in Fig. 23(b) and point A in Fig. 26(a). However, the distribution of pressure coefficients on the downstream surface was not uniform, attributed to intermittent shedding as fluid flowed axially. Additionally, the distribution of pressure coefficients on the upstream and downstream surfaces was essentially identical when the posture of the underwater manipulator was symmetrical, either axisymmetric or origin-symmetric.

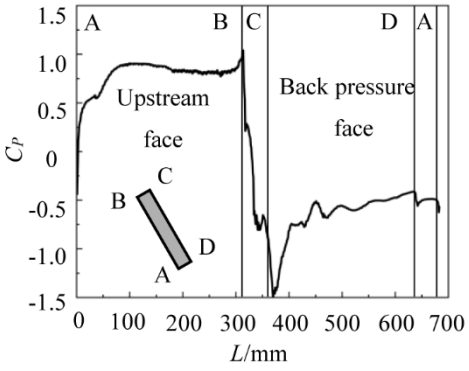

(a) α= -30°

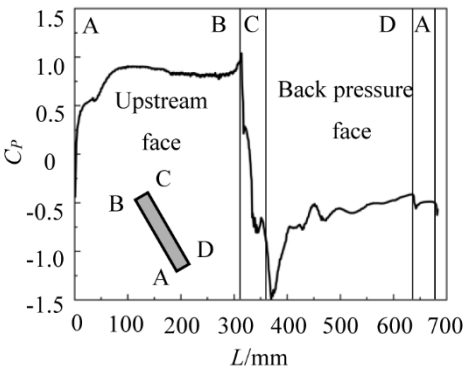

(b) α= 30°

Fig. 23 Axial pressure coefficient in the longitudinal section of the upper arm at α= -30° and α= 30°

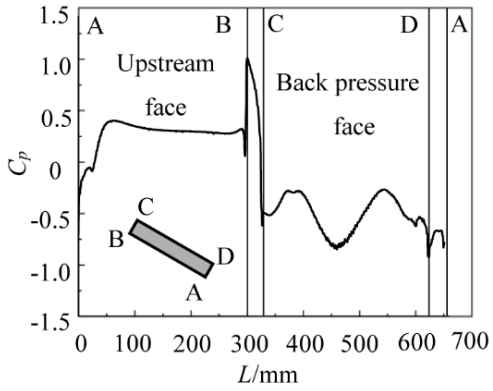

(a) α= -60°

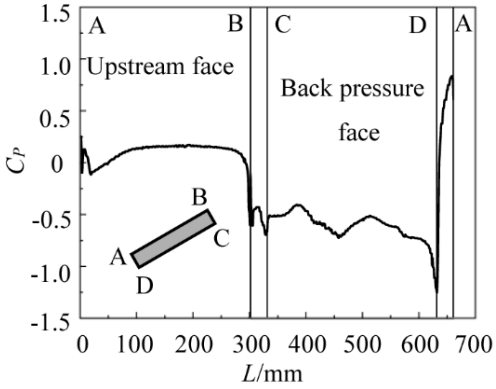

(b) α= 60°

Fig. 24 Axial pressure coefficient in the longitudinal section of the upper arm at α= -60° and α= 60°

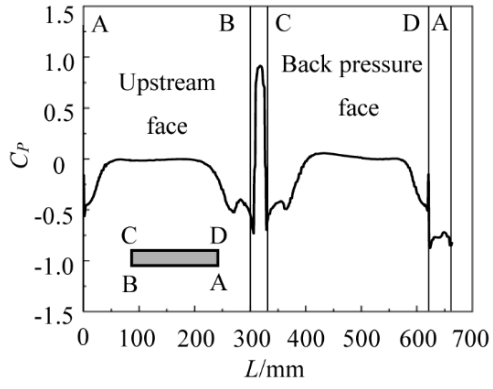

(a) α= -90°

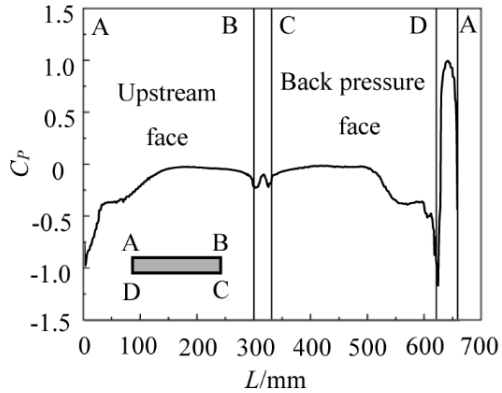

(b) α= 90°

Fig. 25 Axial pressure coefficient in the longitudinal section of the upper arm at α= -90° and α= 90°

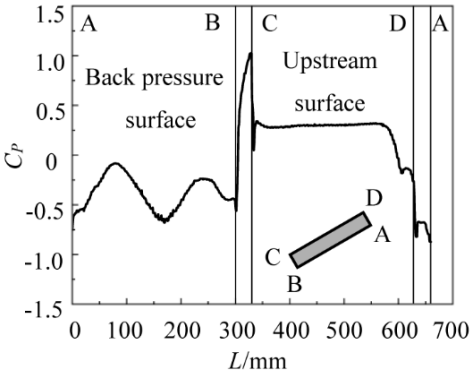

(a) α= -120°

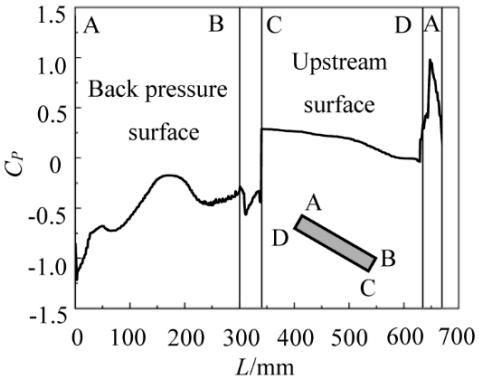

(b) α= 120°

Fig. 26 Axial pressure coefficient in the longitudinal section of the upper arm at α= -120° and α= 120°

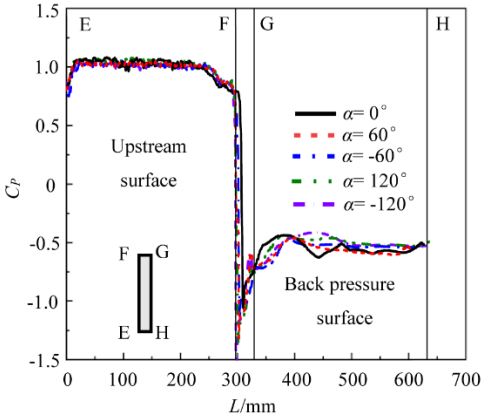

Fig. 27 Axial pressure coefficient distribution on the lower arm at different postures of the upper arm

Numerically, the pressure coefficient on the upstream surface decreased as the angle of the underwater manipulator relative to the *z*-axis increased within the same range of angles (e.g., 0° to -90°). In Figs. 23(b) and 24(b), as the posture angle shifted from 30° to 60°, the upstream pressure coefficient of the surface dropped from 0.75 to 0.25. Similarly, the pressure coefficient on the downstream surface decreased as the angle of the manipulator to the *z*-axis increased, narrowing the reduction was not as large as for the upstream surface. The pressure coefficient differential between upstream and downstream surfaces as the posture angle widened.

Figure 27 shows the axial pressure coefficient profiles in the longitudinal section of the lower arm with the upper

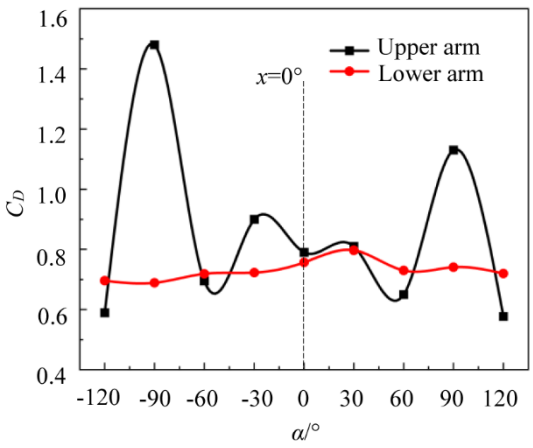

Fig. 28 Drag coefficients of the upper and lower arms in different postures

arm in different postures, indicating that upper arm rotation slightly influenced the pressure coefficient near the tip of the lower arm, an effect so minor it could be disregarded. Therefore, when the upper arm was not in the same plane of rotation as the lower arm, the variation in the posture of the upper arm has little effect on the hydrodynamic force of the lower arm.

3.6 Drag Coefficient in Different Postures

Figure 28 presents the drag coefficients of the entire upper and lower arms for various upper arm postures. The hydrodynamic drag coefficient of the upper arm peaked 1.48 at α= −90°, with the symmetric posture α= 90° exhibiting a smaller value. The drag coefficient of the lower arm remained relatively unchanged with change with variations in the posture of the upper arm. On the contrary, the drag coefficient of the upper arm varied with its posture. Additionally, the pattern of change was consistent on both sides of the *z*-axis, initially increasing then decreasing, mirroring findings from inclined cylindrical column studies by Vakil and Green (2009). Coupled with the axial pressure coefficient curve in Fig. 25(a), it was evident that at α= -90° posture, the downstream surface was affected by the flow field a top the lower arm, diminishing pressure near the end surface and consequently enlarging the pressure difference, thereby, augmenting the drag coefficient.

4. CONCLUSIONS

This paper investigated the hydrodynamic characteristics of an underwater manipulator using numerical methods, focusing on the impact of posture and Reynolds number on flow structure, pressure distribution, and drag coefficient. The findings demonstrated that:

(1) Near the free end of the underwater manipulator in a vertical posture, the Karman vortex street was absent due to axial fluid flow at the end face. Additionally, changes in the posture of the upper arm did not influence the hydrodynamic characteristics of the lower arm.

(2) At a 90° angle of attack from the incoming flow, the Karman vortex street near the end of the underwater manipulator was disrupted by axial fluid flow on the end face. With rotation, axial flow extended over the entire downstream surface, eliminating the Karman vortex street entirely.

(3) The pressure coefficient on the downstream surface of the underwater manipulator increased with the Reynolds number within the range of 6.0×10^3 to 3.0×10^4, whereas the pressure coefficient on the upstream surface remained unchanged. The drag coefficients for the upper and lower arms decreased by 27.4% and 23.9%, respectively.

(4) When the posture of the underwater manipulator was axisymmetric or origin-symmetric, the flow field structure, pressure distribution, and drag coefficient were similar. The highest drag coefficient recorded was 1.48 at a deflection angle of α= −90°.

In conclusion, the insights of this study into the hydrodynamic coefficient and flow field structure of the underwater manipulator contribute to a more accurate theoretical foundation for developing the hydrodynamic model of the manipulator. Future research could expand to investigate different flow dynamics.

ACKNOWLEDGEMENTS

This project is supported by National Natural Science Foundation of China (No.51905211) and A Project of the "20 Regulations for New Universities" funding program of Jinan (No.202228116).

CONFLICT OF INTEREST

We declare that we do not have any commercial or associative interest that represents a conflict of interest in connection with our work submitted.

AUTHORS CONTRIBUTION

Senliang Dai: Methodology, Validation, Investigation, Writing-original draft. **Shanbin Ren**: Formal analysis, Data curation, Writing-original draft. **Xin Liu**: Formal analysis, Data curation. **Derong Duan**: Conceptualization, Formal analysis, Writing-review & editing. **Huifang Jin**: Investigation. **Hui Zhang**: Resources, Supervision.

REFERENCES

Alzabari, F., Wilson, C. A., & Ouro, P. (2023). Unsteady vortex shedding dynamics behind a circular cylinder in very shallow free-surface flows. *Computers & Fluids*, *260*, 105918. https://doi.org/10.1016/j.compfluid.2023.105918.

Avila, J. P. J., Maruyama, N., & Adamowski, J. C. (2008). Hydrodynamic parameter estimation of an open frame unmanned underwater vehicle. *IFAC Proceedings Volumes*, *41*(2), 10504-10509. https://doi.org/10.3182/20080706-5-kr-1001.01779.

Cakir, E., Akinturk, A., & Allievi, A. (2015, May -June). *A numerical study of fluid structure interaction of a flexible submerged cylinder mounted on an*

experimental rig. Proceedings of the ASME 2015 34th International Conference on Ocean, Offshore and Arctic Engineering. St. John's, Newfoundland, Canada. https://doi.org/10.1115/omae2015-42219.

Carlucho, I., Stephens, D. W., & Barbalata, C. (2021). An adaptive data-driven controller for underwater manipulators with variable payload. *Applied Ocean* Research, *113*, 102726. https://doi.org/10.1016/j.apor.2021.102726.

Chen, H. L., Dai, S. S., Li, J., & Yao, X. L. (2009). Three-dimensional numerical simulation of the flow past a circular cylinder based on LES method. *Journal of Marine Science and Application*, *2*(8), 110-116. https://doi.org/10.1007/s11804-009-8110-4.

Cheng, Y., Duan, D., Liu, X., Yang, X., Zhang, H., & Han, Q. (2022). Numerical study on hydrodynamic performance of underwater manipulator in the subcritical region. *Ocean Engineering*, *262*, 112214. http://doi.org/10.1016/j.oceaneng.2022.112214.

Duan, D., Cheng, Y., Liu, X., Yang, X., Zhang, H., & Han, Q. (2023a). Study on the effect of inflow direction on the hydrodynamic characteristics of underwater manipulators. *Ocean Engineering*, *284*, 115221. http://doi.org/10.1016/j.oceaneng.2023.115221.

Duan, D., Ren, S., Zhang, Y., Cheng, Y., Wang, X., & Zhang, H. (2023b). Hydrodynamic coefficients for various postures of the underwater manipulator. *Journal of Applied Fluid Mechanics*, *17*(2), 461-473. http://doi.org/10.47176/jafm.17.02.2085.

Franzini, G. R., Fujarra, A. L. C., Meneghini, J. R., Korkischko, I., & Franciss, R. (2009). Experimental investigation of vortex-induced vibration on rigid, smooth and inclined cylinders. *Journal of Fluids and Structures*, *25*(4), 742-750. http://doi.org/j.jfluidstructs.2009.01.003.

Gao, W., Nelias, D., Liu, Z., & Lyu, Y. (2018). Numerical investigation of flow around one finite circular cylinder with two free ends. *Ocean Engineering*, *156*, 373-380. http://doi.org/10.1016/j.oceaneng.2018.03.020.

Gao, Y., He, J., Ong, M. C., Zhao, M., & Wang, L. (2021). Three-dimensional numerical investigation on flow past two side-by-side curved cylinders. *Ocean Engineering*, *234*, 109167. http://doi.org/10.1016/j.oceaneng.2021.109167.

He, S., & Seddighi, M. (2013). Turbulence in transient channel flow. *Journal of Fluid Mechanics*, *715*, 60-102. http://doi.org/10.1017/jfm.2012.498.

He, S., & Seddighi, M. (2014). Transition of transient channel flow after a change in Reynolds number. *Journal of Fluid Mechanics*, *764*, 395-427. http://doi.org/10.1017/jfm.2014.698.

Hölscher, N., & Niemann, H. J. (1996). Turbulence and separation induced pressure fluctuations on a finite circular cylinder—application of a linear unsteady strip theory. *Journal of Engineering and Industrial Aerodynamics*, *65*(1-3), 335-346. https://doi.org/10.1016/j.oceaneng.2011.09.019.

Hu, G., Tse, K. T., & Kwok, K. C. (2016). Aerodynamic mechanisms of galloping of an inclined square cylinder. *Journal of Wind Engineering and Industrial Aerodynamics*, *148*, 6-17. https://doi.org/10.1016/j.jweia.2015.10.011.

Jung, S. Y., & Chung Y. M. (2012) Large-eddy simulation of accelerated turbulent flow in a pipe. *International Journal of Heat and Fluid Flow*, *33*(1), 1-8. https://doi.org/10.1016/j.ijheatfluidflow.2011.11.005 .

Kawamura, T., Mayer, S., Garapon, A., & Sørensen, L., (2002). Large eddy simulation of a flow past a free surface piercing circular cylinder. *Journal of Fluids Engineering*, *124*(1), 91-101. https://doi.org/10.1115/1.1431545.

Kharghani, M., & Pasandidehfard, M. (2022). Turbulence structures in accelerated flow over a flat plate with non-zero pressure gradient. *Journal of Applied Fluid Mechanics*, *15*(2), 311-324. http://doi.org/10.47176/jafm.15.02.32337.

Kolodziejczyk, W. (2015). Preliminary study of hydrodynamic load on an underwater robotic manipulator. *Journal of Automation Mobile Robots and Intelligent Systems*, *9*. https://doi.org/10.14313/JAMRIS_4-2015/28.

Kolodziejczyk, W. (2016). Some considerations on an underwater robotic manipulator subjected to the environmental disturbances caused by water current. *Acta Mechanica et Automatica*, *10*(1), 43-49. https://doi.org/10.1515/ama-2016-0008.

Kolodziejczyk, W. (2018). The method of determination of transient hydrodynamic coefficients for a single DOF underwater manipulator. *Ocean Engineering*, *153*, 122-131. https://doi.org/10.1016/j.oceaneng.2018.01.090.

Kolodziejczyk, W., Kolodziejczyk, M., Kuzmierowski, T., & Ostaszewski, M. (2023). Transient hydrodynamic coefficient for a single DOF underwater manipulator of square cross-section. *Ocean Engineering*, *268*, 113438. https://doi.org/10.1016/j.oceaneng.2022.113438.

Liang, S. Z., Zhou, J. W., & Mei, L. (2021). Experiments and numerical simulations of the three-dimensional flow around a finite-length circular cylinder. *Ship Science and Technology*, *43*(11), 19-24. http://doi.org/10.3404/j.issn.1672-7649.2021.06.004.

Liu, P., Shen, D., Ba, Y., Cao, J., Liu, J., & Wang, L., (2022). Development and control strategy of subsea all-electric actuators. *Journal of Ocean University of China*, *21*(5), 1133-1146. https://doi.org/10.1007/s11802-022-4928-z.

McLain, T. W., & Rock, S. M. (1998). Development and experimental validation of an underwater manipulator hydrodynamic model. *The International Journal of*

Robotics Research, *17*(7), 748-759. https://doi.org/10.1177/027836499801700705.

Menter, F. (1993, July). *Zonal two equation k-ω turbulence models for aerodynamic flows*. 23rd Fluid Dynamic, Plasmadynamics, and Lasers Conference. Orlando, Florida, USA. https://doi.org/10.2514/6.1993-2906.

Okamoto, T., & Yagita, M. (1973). The experimental investigation on the flow past a circular cylinder of finite length placed normal to the plane surface in a uniform stream. *Bulletin of JSME*, *16*(95), 805-814. http://doi.org/10.1299/jsme1958.16.805.

Park, C. W., & Lee, S. J. (2000). Free end effects on the near wake flow structure behind a finite circular cylinder. *Journal of Wind Engineering and Industrial Aerodynamics*, *88*(2-3), 231-246. http://doi.org/10.1016/s0167-6105(00)00051-9.

Park, C. W., & Lee, S. J. (2004). Effects of free-end corner shape on flow structure around a finite cylinder. *Journal of Fluids and Structures*, *19*(2), 141-158. https://doi.org/10.1016/j.jfluidstructs.2003.12.

PasandidehFard, M., & Naeimirad, M. (2022). Turbulence transient boundary layer over a flat plate. *Ocean Engineering*, *244*, 110192. http://doi.org/10.1016/j.oceaneng.2021.110192.

Pattenden, R. J., Bressloff, N. W., Turnock, S. R., & Zhang, X., (2007). Unsteady simulations of the flow around a short surface-mounted cylinder. *International Journal for Numerical Methods in Fluids*, *53*(6), 895-914. https://doi.org/10.1002/fld.1309.

Roh, S. C., & Park, S. (2003). Vortical flow over the free end surface of a finite circular cylinder mounted on a flat plate. *Experiments in Fluids*, *34*(1), 63-67. https://doi.org/10.1007/s00348-002-0532-6.

Schjølberg, I., & Egeland, O. (1995). Motion control of underwater vehicle-manipulator systems using feedback linearization. *IFAC Proceedings Volumes*. 28(2), 54-59. https://doi.org/10.1016/S1474-6670(17)51651-1.

Sumner, D. (2013). Flow above the free end of a surface-mounted finite-height circular cylinder: A review. *Journal of Fluids and Structures*, *43*, 41-63. https://doi.org/10.1016/j.jfluidstructs.2013.08.007.

Sumner, D., & Heseltine, J. L. (2008). Tip vortex structure for a circular cylinder with a free end. *Journal of Wind Engineering and Industrial Aerodynamics*. *96*(6-7), 1185-1196. https://doi.org/10.1016/j.jweia.2007.06.039.

Suzuki, H., Sakaguchi, J., Inoue, T., Watanabe, Y., & Yoshida, H. (2013). Evaluation of methods to estimate hydrodynamic force coefficients of underwater vehicle based on CFD. *IFAC Proceedings Volumes*, *46*(33), 197-202. https://doi.org/10.3182/20130918-4-jp-3022.00026.

Tsukrov, I., Drach, A., DeCew, J., Swift, M. R., & Celikkol, B. (2011). Characterization of geometry and normal drag coefficients of copper nets. *Ocean Engineering*, *38*(17-18), 1979-1988. https://doi.org/10.1016/i.oceaneng.2011.09.019.

Vakil, A., & Green, S. I. (2009). Drag and lift coefficients of inclined finite circular cylinders at moderate Reynolds numbers. *Computers & Fluids*, *38*(9), 1771-1781. http://doi.org/10.1016/j.compfluid.2009.03.006.

Xu, S., Wu, J., Yang, X., & Zhang, S. (2021). Trajectory tracking and hydrodynamics of a tethered underwater vehicle based on hybrid grid. Ocean Engineering, 241, 110051. https://doi.org/10.1016/j.oceaneng.2021.110051.

Wang, R., Xin, D., & Ou, J. (2020). Three-dimensional characteristics and axial flow pattern in the wake flow of an oblique circular cylinder. *Journal of Wind Engineering and Industrial Aerodynamics*, *206*, 104381. https://doi.org/10.1016/j.jweia.2020.104381.

Wang, X. C., Gui, H. B., & Liu, Y. (2018). Numerical simulation of three-dimensional flow around a circular cylinder of finite length. *Chinese Journal of Ship Research*, *13*(02), 27-34. http://doi.org/10.3969/j.issn.1673-3185.2018.02.004.

Wang, X., Huang, Q., & Pan, G. (2021). Numerical research on the influence of sail leading edge shapes on the hydrodynamic noise of a submarine. *Applied Ocean Research*, *117*, 102935. https://doi.org/10.1016.j.apor.2021.102935.

Wu, Y., Ta, X., Xiao, R., Wei, Y., An, D., & Li, D. (2019). Survey of underwater robot positioning navigation. *Applied Ocean Research*, *90*, 101845. https://doi.org/10.1016/j.apor.2019.06.002.

Yu, H., & Thé, J. (2016). Validation and optimization of SST k-ω turbulence model for pollutant dispersion within a building array. *Atmosphere Environment*, *145*, 225-238. https://doi.org/10.1016/j.atmosenv.2016.09.043.

Zdravkovich, M. M., Brand, V. P., Mathew, G., & Weston, A. (1989). Flow past short circular cylinders with two free ends. *Journal of Fluid Mechanics*, *203*, 557-575. http://doi.org/10.1017/S002211208900159X.

Zhang, M., Liu, X., & Tian, Y. (2019). Modeling analysis and simulation of viscous hydrodynamic model of single-DOF manipulator. *Journal of Marine Science and Engineering*, *7*(8), 261. https://doi.org/10.3390/jmse7080261.

Zhang, Z., Ji, C., Chen, W., Hua, Y., & Srinil, N. (2021). Influence of boundary layer thickness and gap ratios on three-dimensional flow characteristics around a circular cylinder in proximity to a bottom plane. *Ocean Engineering*, *226*, 108858. http://doi.org/10.1016/j.oceaneng.2021.108858.